

PCCP

Accepted Manuscript



This is an *Accepted Manuscript*, which has been through the Royal Society of Chemistry peer review process and has been accepted for publication.

Accepted Manuscripts are published online shortly after acceptance, before technical editing, formatting and proof reading. Using this free service, authors can make their results available to the community, in citable form, before we publish the edited article. We will replace this *Accepted Manuscript* with the edited and formatted *Advance Article* as soon as it is available.

You can find more information about *Accepted Manuscripts* in the [Information for Authors](#).

Please note that technical editing may introduce minor changes to the text and/or graphics, which may alter content. The journal's standard [Terms & Conditions](#) and the [Ethical guidelines](#) still apply. In no event shall the Royal Society of Chemistry be held responsible for any errors or omissions in this *Accepted Manuscript* or any consequences arising from the use of any information it contains.

Cite this: DOI: 10.1039/xxxxxxxxxx

Laser-induced electron localization in H_2^+ : Mixed quantum-classical dynamics based on the exact time-dependent potential energy surface

Yasumitsu Suzuki,^{a†} Ali Abedi,^{ab‡} Neepa T. Maitra,^b and E.K.U. Gross^{ac}

Received Date

Accepted Date

DOI: 10.1039/xxxxxxxxxx

www.rsc.org/journalname

We study the exact nuclear time-dependent potential energy surface (TD PES) for laser-induced electron localization with a view to eventually developing a mixed quantum-classical dynamics method for strong-field processes. The TD PES is defined within the framework of the exact factorization [A. Abedi, N. T. Maitra, and E. K. U. Gross, *Phys. Rev. Lett.* 105, 123002 (2010)] and contains the exact effect of the couplings to the electronic subsystem and to any external fields within a scalar potential. We compare its features with those of the quasistatic potential energy surfaces (QSPES) often used to analyse strong-field processes. We show that the gauge-independent component of the TD PES has a mean-field-like character very close to the density-weighted average of the QSPESs. Oscillations in this component are smoothed out by the gauge-dependent component, and both components are needed to yield the correct force on the nuclei. Once the localization begins to set in, the gradient of the exact TD PES tracks one QSPES and then switches to the other, similar to the description provided by surface-hopping between QSPESs. We show that evolving an ensemble of classical nuclear trajectories on the exact TD PES accurately reproduces the exact dynamics. This study suggests that the mixed quantum-classical dynamics scheme based on evolving multiple classical nuclear trajectories on the exact TD PES will be a novel and useful method to simulate strong field processes.

1 Introduction

With the advent of attosecond technology^{1–6}, the experimentally accessible time-scale has shifted to that of electronic motion. It allows the observation of electronic motion in real-time, and even offers the control of electron motion and localization via lasers. Several groups^{7–26} have demonstrated that it is possible to control electronic motion in a dissociating molecule and localize it selectively on one of the products of dissociation, with several different strategies. One technique employs the carrier envelope phase (CEP) of a single few-cycle laser pulse^{18–25}, and another employs the time-delay between two coherent ultrashort pulses^{7–17}.

These experiments so far treat small systems (such as H_2 and

D_2), with the aim of understanding the mechanisms of localization, before applying the techniques to the control of larger systems^{27,28}. Theoretical studies have a dual role^{7–26}: (i) to help understand the complex correlation between the electron dynamics and nuclear dynamics, and (ii) to establish methods, generally extendable to larger systems, that accurately simulate the coupled electron-nuclear dynamics. For systems with more than two or three degrees of freedom, we must rely on approximate methods, and usually some kind of mixed quantum-classical approach is appropriate, where the electrons are treated quantum-mechanically, coupled to nuclei described via classical trajectories^{29–32}. Different mixed quantum-classical schemes such as Ehrenfest and surface-hopping^{33–35}, differ in their treatment of the classical nuclear motion, but use the same form for the potential acting on the electrons. For dynamics in strong fields, a surface-hopping scheme between quasi-static potential energy surfaces (QSPES) was introduced^{36–38}, and in fact applied to the electron-localization problem¹³. Surface-hopping is known to suffer from over-coherence^{39–46}, but it was shown to reproduce experimental asymmetries reasonably well for this problem.

In this paper, we will study the possibility of using a potential derived from first-principles, the time-dependent potential energy surface (TD PES)^{47,48}, in a mixed quantum-classical description of

^aMax-Planck Institut für Mikrostrukturphysik, Weinberg 2, D-06120 Halle, Germany

^bDepartment of Physics and Astronomy, Hunter College and the City University of New York, 695 Park Avenue, New York, New York 10065, USA

^cEuropean Theoretical Spectroscopy Facility (ETSF)

[†]Present address: Department of Physics, Tokyo University of Science, 1-3 Kagurazaka, Shinjuku-ku, Tokyo 162-8601, Japan

[‡]Present address: Nano-Bio Spectroscopy Group, Departamento Física de Materiales, Universidad del País Vasco, Centro de Física de Materiales CSIC-UPV/EHU-MPC and DIPIC, Avenida Tolosa 72, E-20018 San Sebastian, Spain

the coupled dynamics. This potential arises out of the exact factorization framework where a time-dependent Schrödinger equation (TDSE) for the nuclei alone can be formulated and applications of the approach to real systems are emerging⁴⁹. The potentials appearing in this equation capture exactly all coupling to the electronic system as well as any external fields, and the resulting nuclear wavefunction reproduces the exact nuclear dynamics. The scalar potential is denoted the TDPEs, and in many situations, including all one-dimensional problems, the TDPEs is the *only* potential acting on the nuclear subsystem^{50,51}; its gradient therefore yields the exact force on the nuclei. For this reason, it is important to gain an understanding of its structure, to address both points (i) and (ii) above. Therefore, our aim in this paper is to find the exact TDPEs for the problem of laser-induced electron localization in a one-dimensional model of H_2^+ , compare its structure with potential surfaces more traditionally used for strong-field dynamics, and study classical nuclear dynamics on the exact TDPEs with a view to developing mixed quantum-classical schemes based on the exact factorization.

Previous work^{52–54} has analysed the structure of the exact TDPEs for a case of field-free dynamics, non-adiabatic charge-transfer in the Shin-Metiu model⁵⁵, finding that much intuition is gained by analysing it in term of the Born-Oppenheimer (BO) potential energy surfaces (BOPEs), and that such an analysis enables connections to be made with traditional approximate methods for coupled electron-ion dynamics, such as surface-hopping. Further, it was found that evolving an ensemble of classical nuclear trajectories on the exact TDPEs accurately reproduces the exact nuclear dynamics⁵⁴.

We will show here that analogous conclusions can be drawn for the laser-induced electron localization problem: an ensemble of classical nuclear trajectories evolving on the exact TDPEs accurately reproduces the exact nuclear dynamics, and analysis in terms of the QSPESs, which play the role of the BOPEs when strong fields are present, is helpful. The TDPEs naturally separates into a gauge-independent part and a gauge-dependent part. We show that the density-weighted average of the QSPESs approximates the gauge-independent component, which is rather oscillatory and the force on the nuclei resulting from its gradient is incorrect. Once the gauge-dependent component of the TDPEs is included, the oscillations smoothen out: together, they yield the correct force on the nuclei. Further, we find that, once localization begins to set in, the gradient of the exact TDPEs at the location of the mean nuclear position, tracks that of one QSPES and then switches to the other, resembling the picture provided by the semiclassical surface-hopping approach^{13,37,38}.

A multiple trajectory Ehrenfest dynamics simulation shows that although the nuclear dynamics is reasonably reproduced, an incorrect electron localization asymmetry is obtained. The error can be related to the incorrect BO projections of the electronic wavefunction. The fact that the Ehrenfest dynamics yields inaccurate electron dynamics can be anticipated from our recent work on the exact *electronic*-TDPEs⁵⁶: in this complementary picture, instead of asking what is the exact potential acting on nuclei in an exact TDSE for nuclei, one asks what is the exact potential acting on electrons in an exact TDSE for the electronic

subsystem. We found⁵⁶ that the exact electronic-TDPEs is significantly different from the potential acting on electrons in the usual mixed quantum-classical schemes – including Ehrenfest as well as surface-hopping schemes – yielding significant errors in the prediction of the electron localization asymmetry. The results of the present paper suggest that, instead, mixed quantum-classical schemes based on evolving multiple classical trajectories on the exact TDPEs (or good approximations to it) will be a useful method to simulate strong field processes.

This paper is organized as follows. In section 2, we review two different concepts of potential energy surfaces for TD processes in laser fields: the QSPES and the exact TDPEs. In section 3 we compare the features of these potentials for electron localization dynamics in the dissociation of a model H_2^+ molecule induced by time-delayed coherent ultra shortlaser pulses. We show the exact TDPEs gives the correct force acting on nuclei, so evolving multiple classical trajectories on it reproduces the correct nuclear wavepacket dynamics. The force obtained from surface-hopping between QSPESs can approximately reproduce such an exact force once localization begins to set in. We also compute multiple trajectory Ehrenfest dynamics and reveal how it fails to reproduce electron localization dynamics while it reasonably reproduces the nuclear dynamics. In section 4 we summarize the results and remark on the future directions.

2 Theory

2.1 Quasi-static potential energy surface

In this section we first review the concept of the QSPES introduced for the description of molecules in strong-fields. The QSPES has been thoroughly discussed in earlier works^{13,36–38,57–63}, but we here give a discussion particularly relevant for the electron localization dynamics problem in the dissociation of H_2^+ .

For this problem, the essential physics is contained in the two lowest field-free electronic states of the BO Hamiltonian, i.e., the $1s\sigma_g$ and $2p\sigma_u$ states, and the full molecular wavefunction $\Psi(R, \mathbf{r}, t)$ of the system can be expressed as

$$\Psi(R, \mathbf{r}, t) = \chi_g(R, t)\phi_R^g(\mathbf{r}) + \chi_u(R, t)\phi_R^u(\mathbf{r}). \quad (1)$$

Here $\chi_g(R, t)$ and $\chi_u(R, t)$ describe nuclear wavefunctions that exist in the $1s\sigma_g$ and $2p\sigma_u$ states respectively, functions of the internuclear distance R and time t , and $\phi_R^g(\mathbf{r})$ and $\phi_R^u(\mathbf{r})$ describe the $1s\sigma_g$ and $2p\sigma_u$ electronic wavefunction respectively, which parametrically depend on R . Since $\phi_R^g(\mathbf{r})$ and $\phi_R^u(\mathbf{r})$ are bonding and anti-bonding combination of $1s$ atomic orbitals, a coherent superposition of them provides the localized electronic states $\phi_R^{\text{left, right}}(\mathbf{r}) = \frac{1}{\sqrt{2}}(\phi_R^g(\mathbf{r}) \pm \phi_R^u(\mathbf{r}))$ that have the electron on either the left or the right proton. These states form a convenient basis in which to monitor the electron localization asymmetry. In the experiment, interactions of the molecule with the time-delayed infra-red laser field in the course of the dissociation provides a coupling of $\phi_R^g(\mathbf{r})$ and $\phi_R^u(\mathbf{r})$, creating a coherent superposition state, and, instead of Eq. 1, it is instructive to write:

$$\Psi(R, \mathbf{r}, t) = \chi_{\text{left}}(R, t)\phi_R^{\text{left}}(\mathbf{r}) + \chi_{\text{right}}(R, t)\phi_R^{\text{right}}(\mathbf{r}) \quad (2)$$

where $\chi_{\text{left}}(R,t)$ and $\chi_{\text{right}}(R,t)$ are defined as the nuclear wavefunctions that exist in connection with $\phi_R^{\text{left}}(\mathbf{r})$ and $\phi_R^{\text{right}}(\mathbf{r})$. Measurements of ion fragment asymmetries left or right along the polarization axis directly relate to $\chi_{\text{left}}(R,t)$ and $\chi_{\text{right}}(R,t)$.

While the field-free states above are useful to analyse the asymmetry, to understand the time-development of the localization it is helpful to consider a third, time-dependent, basis, the TD quasistatic states, $\phi_R^{\text{QS}(i)}(\mathbf{r},t)$, also known as phase-adiabatic states. These states are defined as instantaneous eigenstates of the instantaneous electronic Hamiltonian $\hat{H}_R^{\text{int}}(\mathbf{r},t)$, defined by

$$\hat{H}_R^{\text{int}}(\mathbf{r},t) = \hat{H}_R^{\text{BO}}(\mathbf{r}) + \hat{v}_{\text{laser}}(\mathbf{r},t), \quad (3)$$

i.e.,

$$\hat{H}_R^{\text{int}}(\mathbf{r},t)\phi_R^{\text{QS}(i)}(\mathbf{r},t) = \varepsilon^{\text{QS}(i)}(R,t)\phi_R^{\text{QS}(i)}(\mathbf{r},t) \quad (4)$$

where $\varepsilon^{\text{QS}(i)}(R,t)$ are the quasistatic potential energy surfaces (QSPEs). Within our two-state model we may write

$$\phi_R^{\text{QS}(i)}(\mathbf{r},t) = c_g^{(i)}(R,t)\phi_R^g(\mathbf{r}) + c_u^{(i)}(R,t)\phi_R^u(\mathbf{r}), \quad (5)$$

so that the $\varepsilon^{\text{QS}(i)}(R,t)$ of Eq. (4) are given by the eigenvalue equation:

$$\begin{pmatrix} \langle \phi_R^g | \hat{H}_R^{\text{int}} | \phi_R^g \rangle & \langle \phi_R^g | \hat{H}_R^{\text{int}} | \phi_R^u \rangle \\ \langle \phi_R^u | \hat{H}_R^{\text{int}} | \phi_R^g \rangle & \langle \phi_R^u | \hat{H}_R^{\text{int}} | \phi_R^u \rangle \end{pmatrix} \begin{pmatrix} c_g^{(i)} \\ c_u^{(i)} \end{pmatrix} = \varepsilon^{\text{QS}(i)} \begin{pmatrix} c_g^{(i)} \\ c_u^{(i)} \end{pmatrix}. \quad (6)$$

Therefore we can express the QSPEs in terms of the BOPEs $\varepsilon^{\text{BO}(i)}(R)$ as

$$\begin{aligned} \varepsilon^{\text{QS}(1,2)}(R,t) = & \varepsilon^{\text{BO}(1,2)}(R) \cos^2 \theta(R,t) + \varepsilon^{\text{BO}(2,1)}(R) \sin^2 \theta(R,t) \\ & \pm \langle \phi_R^g | \hat{v}_{\text{laser}} | \phi_R^u \rangle \sin 2\theta(R,t) \end{aligned} \quad (7)$$

and the electronic quasi-static eigenstates in terms of the BO states,

$$\begin{aligned} \phi_R^{\text{QS}(1)}(\mathbf{r},t) &= \cos \theta(R,t)\phi_R^g(\mathbf{r}) + \sin \theta(R,t)\phi_R^u(\mathbf{r}) \\ \phi_R^{\text{QS}(2)}(\mathbf{r},t) &= \sin \theta(R,t)\phi_R^g(\mathbf{r}) - \cos \theta(R,t)\phi_R^u(\mathbf{r}), \end{aligned} \quad (8)$$

where the TD mixing parameter $\theta(R,t)$ is given by

$$\tan 2\theta(R,t) = \frac{2\langle \phi_R^g | \hat{v}_{\text{laser}} | \phi_R^u \rangle}{\varepsilon^{\text{BO}(1)}(R) - \varepsilon^{\text{BO}(2)}(R)}. \quad (9)$$

The molecular wavefunction expressed in terms of quasi-static states is

$$\Psi(R,\mathbf{r},t) = \chi_1^{\text{QS}}(R,t)\phi_R^{\text{QS}(1)}(\mathbf{r},t) + \chi_2^{\text{QS}}(R,t)\phi_R^{\text{QS}(2)}(\mathbf{r},t). \quad (10)$$

Note that the nuclear wavefunctions $\chi_1^{\text{QS}}(R,t)$ and $\chi_2^{\text{QS}}(R,t)$ are connected to the quasi-static states $\phi_R^{\text{QS}(1)}(\mathbf{r},t)$ and $\phi_R^{\text{QS}(2)}(\mathbf{r},t)$

can be expressed in terms of $\chi_{\text{left}}(R,t)$ and $\chi_{\text{right}}(R,t)$ as

$$\begin{aligned} \chi_1^{\text{QS}}(R,t) &= \frac{1}{\sqrt{2}}[\chi_{\text{left}}(R,t)(\cos \theta + \sin \theta) \\ &\quad + \chi_{\text{right}}(R,t)(\cos \theta - \sin \theta)] \\ \chi_2^{\text{QS}}(R,t) &= \frac{1}{\sqrt{2}}[\chi_{\text{left}}(R,t)(-\cos \theta + \sin \theta) \\ &\quad + \chi_{\text{right}}(R,t)(\cos \theta + \sin \theta)]. \end{aligned} \quad (11)$$

which can be used to extract the electron localization from $\chi_1^{\text{QS}}(R,t)$ and $\chi_2^{\text{QS}}(R,t)$.

A semi-classical surface-hopping model based on QSPEs has recently been utilized to understand and reproduce the electron localization dynamics and asymmetry^{13,37,38} in H_2^+ . In this approach, an ensemble of classical nuclear trajectories evolve on one QSPE or the other QSPE, making instantaneous hops between them as determined by a Landau-Zener formula. It was shown that the electron localization sets in a region where the dynamics is intermediate between adiabatic and diabatic: the ensemble of nuclear trajectories traverses several laser-induced avoided crossings between the QSPEs. This semi-classical method gives asymmetry parameters in reasonably good overall agreement with that obtained from the full TDSE although the details differ. The agreement lends some hope to the use of this semiclassical scheme to simulate coupled electron-ion dynamics in control problems of more complicated systems; however, at the same time a further understanding of the errors in the details is desirable. We will analyse this approach by comparing the QSPEs with the exact TDPEs, which we will review in the next section.

2.2 Exact time-dependent potential energy surface

In Ref.^{47,48}, it was shown that the full molecular wavefunction $\Psi(\underline{\mathbf{r}}, \underline{\mathbf{R}}, t)$ which solves the TDSE

$$\hat{H}\Psi(\underline{\mathbf{r}}, \underline{\mathbf{R}}, t) = i\partial_t\Psi(\underline{\mathbf{r}}, \underline{\mathbf{R}}, t) \quad (12)$$

can be exactly factorized to the single product

$$\Psi(\underline{\mathbf{r}}, \underline{\mathbf{R}}, t) = \chi(\underline{\mathbf{R}}, t)\Phi_{\underline{\mathbf{R}}}(\underline{\mathbf{r}}, t) \quad (13)$$

of the nuclear wavefunction $\chi(\underline{\mathbf{R}}, t)$ and the electronic wavefunction $\Phi_{\underline{\mathbf{R}}}(\underline{\mathbf{r}}, t)$ that parametrically depends on the nuclear positions $\underline{\mathbf{R}}$ and satisfies the partial normalization condition

$$\int d\underline{\mathbf{r}} |\Phi_{\underline{\mathbf{R}}}(\underline{\mathbf{r}}, t)|^2 = 1 \quad \forall \underline{\mathbf{R}}, t. \quad (14)$$

Here, the complete molecular Hamiltonian is

$$\hat{H} = \hat{T}_n(\underline{\mathbf{R}}) + \hat{V}_{\text{ext}}^n(\underline{\mathbf{R}}, t) + \hat{H}_{\text{BO}}(\underline{\mathbf{r}}, \underline{\mathbf{R}}) + \hat{v}_{\text{ext}}^e(\underline{\mathbf{r}}, t), \quad (15)$$

and $\hat{H}_{\text{BO}}(\underline{\mathbf{r}}, \underline{\mathbf{R}})$ is the BO electronic Hamiltonian,

$$\hat{H}_{\text{BO}} = \hat{T}_e(\underline{\mathbf{r}}) + \hat{W}_{ee}(\underline{\mathbf{r}}) + \hat{W}_{en}(\underline{\mathbf{r}}, \underline{\mathbf{R}}) + \hat{W}_{nn}(\underline{\mathbf{R}}). \quad (16)$$

Note that $\hat{T}_n = -\sum_{\alpha=1}^{N_n} \frac{\nabla_{\alpha}^2}{2M_{\alpha}}$ and $\hat{T}_e = -\sum_{j=1}^{N_e} \frac{\nabla_j^2}{2m}$ are the nuclear and electronic kinetic energy operators, \hat{W}_{ee} , \hat{W}_{en} and \hat{W}_{nn} are the electron-electron, electron-nuclear and nuclear-nuclear interaction, and $\hat{V}_{ext}^n(\underline{\mathbf{R}}, t)$ and $\hat{v}_{ext}^e(\underline{\mathbf{r}}, t)$ are time-dependent (TD) external potentials acting on the nuclei and electrons, respectively. Throughout this paper $\underline{\mathbf{R}}$ and $\underline{\mathbf{r}}$ collectively represent the nuclear and electronic coordinates respectively and $\hbar = 1$.

Returning to Eq. (13), the stationary variations of the quantum mechanical action with respect to $\Phi_{\underline{\mathbf{R}}}(\underline{\mathbf{r}}, t)$ and $\chi(\underline{\mathbf{R}}, t)$ under the condition (14) lead to the following equations of motion for $\chi(\underline{\mathbf{R}}, t)$ and $\Phi_{\underline{\mathbf{R}}}(\underline{\mathbf{r}}, t)$:

$$\begin{aligned} & \left(\hat{H}_{BO}(\underline{\mathbf{r}}, \underline{\mathbf{R}}) + \hat{v}_{ext}^e(\underline{\mathbf{r}}, t) + \hat{U}_{en}^{coup}[\Phi_{\underline{\mathbf{R}}}, \chi] - \varepsilon(\underline{\mathbf{R}}, t) \right) \Phi_{\underline{\mathbf{R}}}(\underline{\mathbf{r}}, t) \\ & = i\partial_t \Phi_{\underline{\mathbf{R}}}(\underline{\mathbf{r}}, t) \end{aligned} \quad (17)$$

$$\begin{aligned} & \left[\sum_{\alpha=1}^{N_n} \frac{[-i\nabla_{\alpha} + \mathbf{A}_{\alpha}(\underline{\mathbf{R}}, t)]^2}{2M_{\alpha}} + \hat{V}_{ext}^n(\underline{\mathbf{R}}, t) + \varepsilon(\underline{\mathbf{R}}, t) \right] \chi(\underline{\mathbf{R}}, t) \\ & = i\partial_t \chi(\underline{\mathbf{R}}, t). \end{aligned} \quad (18)$$

Here, $\varepsilon(\underline{\mathbf{R}}, t)$ is the exact nuclear TDPES

$$\varepsilon(\underline{\mathbf{R}}, t) = \left\langle \Phi_{\underline{\mathbf{R}}}(t) \left| \hat{H}_{BO} + \hat{v}_{ext}^e(\underline{\mathbf{r}}, t) + \hat{U}_{en}^{coup} - i\partial_t \right| \Phi_{\underline{\mathbf{R}}}(t) \right\rangle_{\underline{\mathbf{r}}}, \quad (19)$$

$\hat{U}_{en}^{coup}[\Phi_{\underline{\mathbf{R}}}, \chi]$ is the ‘‘electron-nuclear coupling operator’’,

$$\begin{aligned} \hat{U}_{en}^{coup}[\Phi_{\underline{\mathbf{R}}}, \chi] &= \sum_{\alpha=1}^{N_n} \frac{1}{M_{\alpha}} \left[\frac{[-i\nabla_{\alpha} - \mathbf{A}_{\alpha}(\underline{\mathbf{R}}, t)]^2}{2} \right. \\ & \left. + \left(\frac{-i\nabla_{\alpha}\chi}{\chi} + \mathbf{A}_{\alpha}(\underline{\mathbf{R}}, t) \right) (-i\nabla_{\alpha} - \mathbf{A}_{\alpha}(\underline{\mathbf{R}}, t)) \right], \end{aligned} \quad (20)$$

and $\mathbf{A}_{\alpha}(\underline{\mathbf{R}}, t)$ is the TD vector potential,

$$\mathbf{A}_{\alpha}(\underline{\mathbf{R}}, t) = \left\langle \Phi_{\underline{\mathbf{R}}}(t) \left| -i\nabla_{\alpha} \Phi_{\underline{\mathbf{R}}}(t) \right\rangle_{\underline{\mathbf{r}}}. \quad (21)$$

The symbol $\langle \cdot \rangle_{\underline{\mathbf{r}}}$ indicates an integration over electronic coordinates only. Note that the PNC makes the factorization (13) unique up to within a $(\underline{\mathbf{R}}, t)$ -dependent gauge transformation,

$$\begin{aligned} \chi(\underline{\mathbf{R}}, t) &\rightarrow \tilde{\chi}(\underline{\mathbf{R}}, t) = e^{-i\theta(\underline{\mathbf{R}}, t)} \chi(\underline{\mathbf{R}}, t) \\ \Phi_{\underline{\mathbf{R}}}(\underline{\mathbf{r}}, t) &\rightarrow \tilde{\Phi}_{\underline{\mathbf{R}}}(\underline{\mathbf{r}}, t) = e^{i\theta(\underline{\mathbf{R}}, t)} \Phi_{\underline{\mathbf{R}}}(\underline{\mathbf{r}}, t) \end{aligned} \quad (22)$$

and Eqs. (17) and (18) are form invariant under this transformation while the scalar potential and the vector potential transform as

$$\tilde{\varepsilon}(\underline{\mathbf{R}}, t) = \varepsilon(\underline{\mathbf{R}}, t) + \partial_t \theta(\underline{\mathbf{R}}, t) \quad (23)$$

$$\tilde{\mathbf{A}}_{\alpha}(\underline{\mathbf{R}}, t) = \mathbf{A}_{\alpha}(\underline{\mathbf{R}}, t) + \nabla_{\alpha} \theta(\underline{\mathbf{R}}, t). \quad (24)$$

The equation for the exact nuclear wavefunction, Eq. (18), is Schrödinger-like, and the TD vector potential (21) and TD scalar potential (19) that appear in it, exactly govern the nuclear dynamics. It is important to note that $\chi(\underline{\mathbf{R}}, t)$ can be interpreted as the exact nuclear wave-function since it leads to an N -body nu-

clear density, $\Gamma(\underline{\mathbf{R}}, t) = |\chi(\underline{\mathbf{R}}, t)|^2$, and an N -body current density, $\mathbf{J}_{\alpha}(\underline{\mathbf{R}}, t) = \frac{1}{M_{\alpha}} \left[\text{Im}(\chi^*(\underline{\mathbf{R}}, t) \nabla_{\alpha} \chi(\underline{\mathbf{R}}, t)) + \Gamma(\underline{\mathbf{R}}, t) \mathbf{A}_{\alpha}(\underline{\mathbf{R}}, t) \right]$, which reproduce the true nuclear N -body density and current density⁴⁸ obtained from the full wave-function $\Psi(\underline{\mathbf{r}}, \underline{\mathbf{R}}, t)$.

In our previous work the shape of this exact TDPES has been useful to interpret dynamics for both a strong field process (strong-field dissociation of H_2^+)^{47,48} as well as for field-free dynamics of non-adiabatic charge-transfer⁵²⁻⁵⁴. In particular, in the field-free case, a detailed study of the form of its gauge-dependent and gauge-independent parts proved instructive to understand its effect on the nuclear dynamics, and the structure to be expected for general field-free problems. Importantly, in a mixed quantum-classical description, the gradient of this exact TDPES gives uniquely the correct force on the nuclei, and it was shown, in the field-free case, that an ensemble of classical trajectories evolving on the exact TDPES accurately reproduces the exact nuclear wavepacket dynamics. We now consider a detailed study of the form of the exact TDPES for the present case of dynamics in external fields, with the aims of addressing three questions. First, does running classical nuclear dynamics on the exact TDPES reproduce the dynamics of laser-induced electron localization? Second, how are the QSPESs related to the exact TDPES? Third, can we see hints of the semiclassical surface-hopping method in the exact TDPES similar to the case of field-free non-adiabatic charge transfer dynamics?

3 Results and discussion

3.1 Theoretical model

We employ a one-dimensional model of the H_2^+ molecule to study electron localization dynamics achieved by time-delayed coherent ultra short laser pulses^{7,8,13}. In the experiment, first an ultraviolet (UV) pulse excites H_2^+ to the dissociative $2p\sigma_u$ state while a second, time-delayed, infrared (IR) pulse induces electron transfer between the dissociating atoms. In our model, we start the dynamics after the excitation by the UV pulse: the wavepacket starts at $t = 0$ on the first excited state ($2p\sigma_u$ state) of H_2^+ as a Frank-Condon projection of the wavefunction of the ground state, and then is exposed to the IR laser pulse. The full Hamiltonian of the system is given by

$$\begin{aligned} \hat{H}(R, z, t) &= \hat{T}_n(R) + \hat{H}_R^{\text{int}}(z, t) \\ &= \hat{T}_n(R) + \hat{T}_e(z) + \hat{W}_{nn}(R) + \hat{W}_{en}(z, R) + \hat{v}_{\text{laser}}(z, t) \end{aligned} \quad (25)$$

where R is the internuclear distance and z is the electronic coordinate as measured from the nuclear center of mass. The kinetic energy terms are $\hat{T}_n(R) = -\frac{1}{2\mu_n} \frac{\partial^2}{\partial R^2}$ and, $\hat{T}_e(z) = -\frac{1}{2\mu_e} \frac{\partial^2}{\partial z^2}$, respectively, where the reduced mass of the nuclei is given by $\mu_n = M_{\text{H}}/2$, and reduced electronic mass is given by $\mu_e = \frac{2M_{\text{H}}}{2M_{\text{H}}+1}$ (M_{H} is the proton mass). The interactions are soft-Coulomb: $\hat{W}_{nn}(R) = \frac{1}{\sqrt{0.03+R^2}}$, and $\hat{W}_{en}(z, R) = -\frac{1}{\sqrt{1.0+(z-\frac{R}{2})^2}} - \frac{1}{\sqrt{1.0+(z+\frac{R}{2})^2}}$ (and $\hat{W}_{ee} = 0$). The IR pulse is described within the dipole approximation and length gauge, as $\hat{v}_{ext}^e(z, t) = E(t)q_e z$, where $E(t) = E_0 \exp\left[-\left(\frac{t-\Delta t}{\tau}\right)^2\right] \cos(\omega(t-\Delta t))$, and the reduced charge

$q_e = \frac{2M_H+2}{2M_H+1}$. The wavelength is 800 nm and the peak intensity $I_0 = E_0^2 = 3.0 \times 10^{12} \text{W/cm}^2$. The pulse duration is $\tau = 4.8 \text{fs}$ and Δt is the time delay between the UV and IR pulses. Here we show the results of $\Delta t = 7 \text{fs}$.

We propagate the full TDSE

$$\hat{H}(z, R, t)\Psi(z, R, t) = i\partial_t\Psi(z, R, t) \quad (26)$$

numerically exactly to obtain the full molecular wavefunction $\Psi(z, R, t)$, and from it we calculate the probabilities of directional localization of the electron, P_{\pm} , which are defined as $P_{+(-)} = \int_{z>(<)0} dz \int dR |\Psi(z, R, t)|^2$. These are shown as the green solid (P_-) and red dashed (P_+) lines in Fig. 1b. It is evident from this figure that considerable electron localization occurs, with the electron density predominantly localized on the left (negative z-axis).

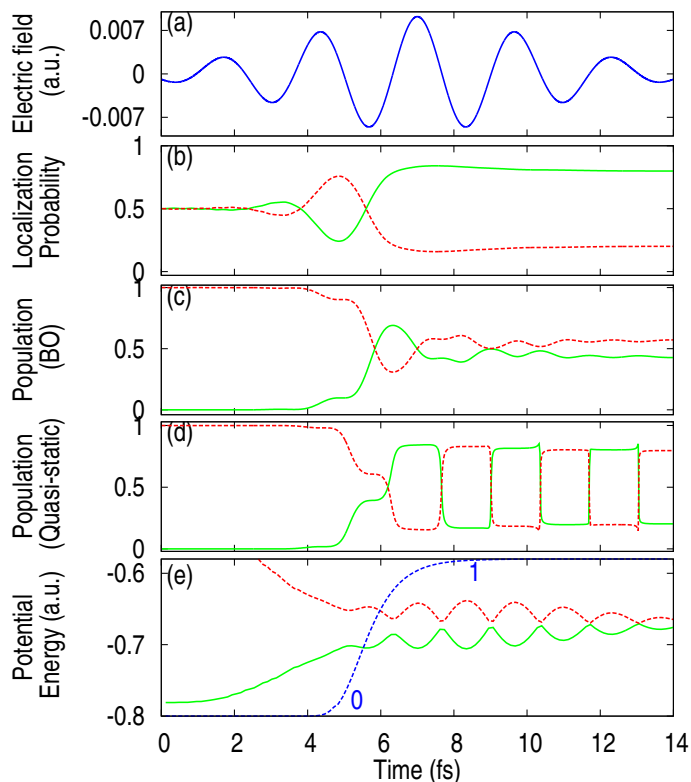


Fig. 1 (a) 4.8 fs FWHM 800 nm laser pulse. (b) Electron localization probabilities along the negative (green solid line) and the positive z-axis (red dashed line) as a function of time. (c) Population dynamics during dissociation on the BO state $\phi_R^g(z)$ (green solid) and $\phi_R^h(z)$ (red dashed). (d) Population dynamics during dissociation on the 1st quasi-static state $\phi_R^{\text{QS}(1)}(z, t)$ (green solid) and 2nd quasi-static state $\phi_R^{\text{QS}(2)}(z, t)$ (red dashed). (e) Quasi-static potential energy surfaces $\epsilon^{\text{QS}(1)}(R, t)$ (green solid) and $\epsilon^{\text{QS}(2)}(R, t)$ (red dashed) for a nuclear trajectory $\langle R(t) \rangle$ that tracks the expectation value of the internuclear distance. The blue curve shows the transition probability given by a Landau-Zener formula (Eq. 18 of Ref. ¹³).

Furthermore, we calculate the population dynamics of the BO states $\phi_R^g(z)$ (green solid) and $\phi_R^h(z)$ (red dashed) (Fig. 1c) during dissociation, as well as the population dynamics on the 1st quasi-static state $\phi_R^{\text{QS}(1)}(z, t)$ (green solid) and 2nd quasi-static state $\phi_R^{\text{QS}(2)}(z, t)$ (red dashed) (Fig. 1d); the relative simplicity of the latter demonstrate the usefulness of the QS basis for laser-induced

processes. We then plot the QSPESs $\epsilon^{\text{QS}(1)}(\langle R(t) \rangle, t)$ (green solid) and $\epsilon^{\text{QS}(2)}(\langle R(t) \rangle, t)$ (red dashed) evaluated at a nuclear trajectory $\langle R(t) \rangle$ that tracks the expectation value of the internuclear distance. These results coincide qualitatively with the previous results reported by Kelkensberg et al.¹³ Panels b, d, and e, suggest that the electron localization is determined by the passage of the dissociating molecule through a regime where the laser-molecule interaction is neither diabatic nor adiabatic. As discussed in the previous section, the semiclassical scheme, with the avoided crossings between the QSPES inducing the trajectories to hop between them, reproduces the general behavior. Next, we will compare the exact TDPEs with the QSPES to understand the relation between the two, shed some light on the surface-hopping scheme, and find the exact force on classical nuclei.

3.2 Exact TDPEs vs. QSPES

First we show the exact TDPEs for this process in Fig. 2. We calculate the TDPEs in the gauge where the vector potential $A(R, t)$ is zero⁴⁸, so the TDPEs $\epsilon(R, t)$ is the only potential acting on the nuclear subsystem. It is instructive to express the TDPEs as the sum of the gauge-independent term $\epsilon_{gi}(R, t)$ and the gauge-dependent term $\epsilon_{gd}(R, t)$ as done in previous studies^{48,52}:

$$\epsilon(R, t) = \epsilon_{gi}(R, t) + \epsilon_{gd}(R, t) \quad (27)$$

where

$$\epsilon_{gi}(R, t) = \langle \Phi_R(t) | \hat{H}_{BO} + \hat{v}_{\text{laser}} + \hat{U}_{\text{en}}^{\text{coup}} | \Phi_R(t) \rangle_z \quad (28)$$

and

$$\epsilon_{gd}(R, t) = \langle \Phi_R(t) | -i\partial_t | \Phi_R(t) \rangle_z. \quad (29)$$

In Fig. 2, $\epsilon(R, t)$ (black solid), $\epsilon_{gi}(R, t)$ (blue solid) and $\epsilon_{gd}(R, t)$ (orange solid) are plotted at nine different times, along with the two lowest BOPEs, $\epsilon^{\text{BO}(1)}(R)$ and $\epsilon^{\text{BO}(2)}(R)$. (Note that the TDPEs $\epsilon(R, t)$ (black solid) and its GD component $\epsilon_{gd}(R, t)$ (orange solid) have been rigidly shifted along the energy axis).

We also plot the exact nuclear density $|\chi(R, t)|^2$ (green solid) and the nuclear density reconstructed from evolving an ensemble of 800 classical trajectories on the exact TDPEs (red dashed)⁵⁴ at each time. The closeness of these last two curves shows that a mixed quantum-classical scheme for the electron localization process is appropriate and that the exact TDPEs $\epsilon(R, t)$ gives the correct force acting on classical nuclei in such a scheme.

In previous work⁵²⁻⁵⁴, step-like features of $\epsilon_{gi}(R, t)$ and $\epsilon_{gd}(R, t)$ in the field-free non-adiabatic process in the vicinity of the avoided crossing have been shown. In particular, after passage through the avoided crossing, where the nuclear wavepacket had spatially separated on two BOPEs, the GI component tracked one BO surface or the other, with a step between them, while the GD component was piecewise flat, but with a step in the same region with opposite sign. The net TDPEs was overall more smooth than either of the components. Here, we find again very interesting features of $\epsilon_{gi}(R, t)$ and $\epsilon_{gd}(R, t)$. First note that both $\epsilon_{gi}(R, t)$ and $\epsilon_{gd}(R, t)$ shows many small hills and valleys after the laser-induced nonadiabatic transitions begin, but with

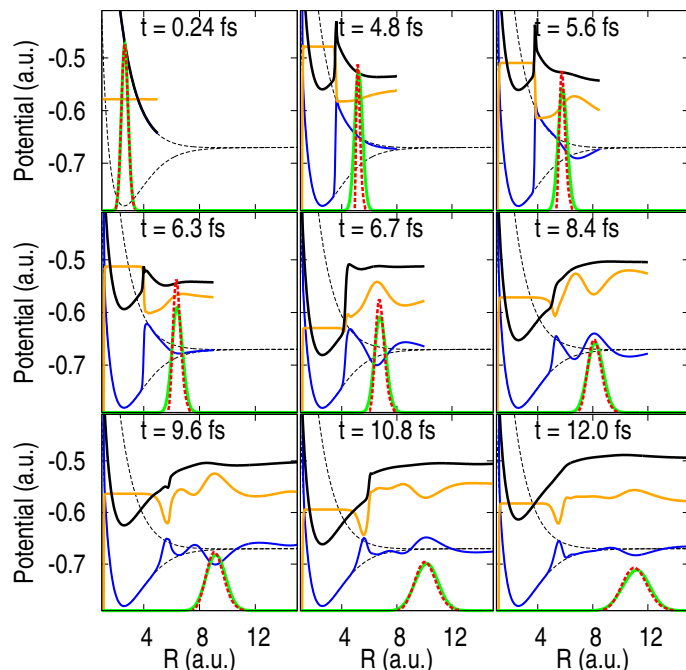


Fig. 2 Snapshot of the exact TD PES $\varepsilon(R,t)$ (black solid), its gauge-invariant part $\varepsilon_{gi}(R,t)$ (blue solid) and gauge-dependent part $\varepsilon_{gd}(R,t)$ (orange solid) at indicated times along with two lowest BOPESs (black dashed). Furthermore, the exact nuclear density $|\chi(R,t)|^2$ (green solid) and the nuclear density reconstructed from the multiple trajectory dynamics on the exact TD PES (red dashed) for each time are also plotted.

opposite slopes to each other, so that these structures largely cancel each other when the exact TD PES $\varepsilon(R,t)$ is constructed (much like the near-cancellation of the steps in the field-free case). Like the field-free case, both the GI and GD terms are important to consider to predict the correct nuclear dynamics. Second, in the present strong-field case, unlike the field-free examples studied in^{52–54}, $\varepsilon_{gi}(R,t)$ does not piecewise track one BOPES or the other. However, it does track a *density-weighted* QSPES, as we will show next.

In Fig. 3, we show $\varepsilon(R,t)$ (black solid) (which is again rigidly shifted along the energy axis) and the gauge-invariant part $\varepsilon_{gi}(R,t)$ (blue solid) together with the QSPESs $\varepsilon^{QS(1)}(R,t)$ (green solid) and $\varepsilon^{QS(2)}(R,t)$ (red solid). We find that the oscillations in the gauge-invariant part of exact TD PES $\varepsilon_{gi}(R,t)$ (blue solid) tend to step between the two QSPESs: $|\chi_1^{QS}(R,t)|^2$ and $|\chi_2^{QS}(R,t)|^2$ are also plotted in Fig. 3, and we see that $\varepsilon_{gi}(R,t)$ tends towards the QSPES whose population is dominant, i.e. when $|\chi_1^{QS}(R,t)|^2$ is larger than $|\chi_2^{QS}(R,t)|^2$ $\varepsilon_{gi}(R,t)$ approaches to $\varepsilon^{QS(1)}(R,t)$ and when $|\chi_2^{QS}(R,t)|^2$ is larger than $|\chi_1^{QS}(R,t)|^2$ $\varepsilon_{gi}(R,t)$ approaches to $\varepsilon^{QS(2)}(R,t)$. In fact, $\varepsilon_{gi}(R,t)$ lies practically on top of the weighted average of the quasi-static surfaces $\varepsilon_{ave}^{QS}(R,t)$:

$$\varepsilon_{ave}^{QS}(R,t) = \frac{|\chi_1^{QS}(R,t)|^2}{|\chi_1^{QS}(R,t)|^2 + |\chi_2^{QS}(R,t)|^2} \varepsilon^{QS(1)}(R,t) + \frac{|\chi_2^{QS}(R,t)|^2}{|\chi_1^{QS}(R,t)|^2 + |\chi_2^{QS}(R,t)|^2} \varepsilon^{QS(2)}(R,t) \quad (30)$$

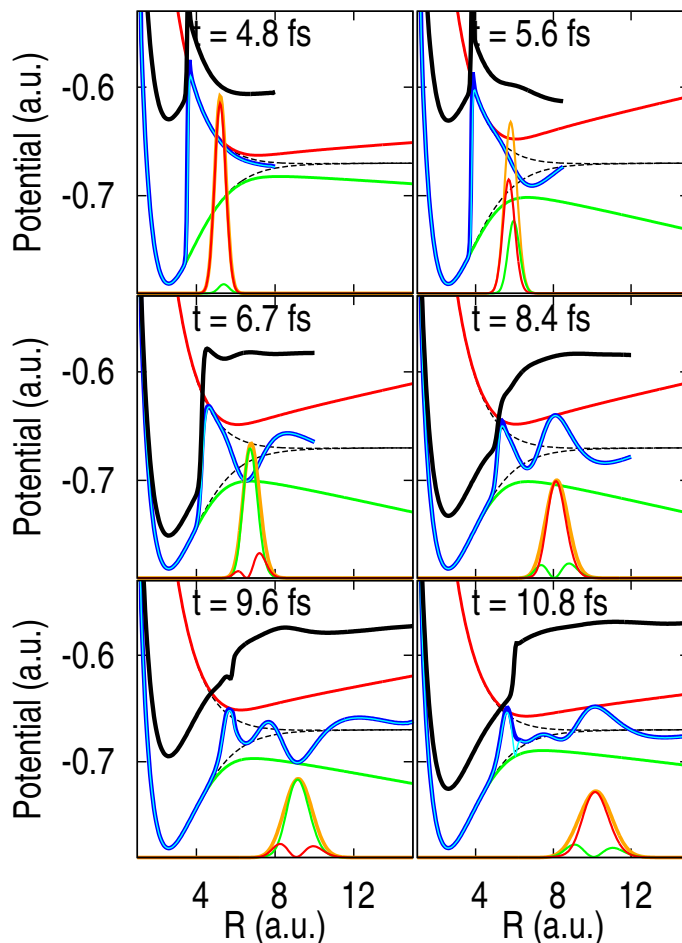


Fig. 3 Snapshots of the exact TD PES $\varepsilon(R,t)$ (black solid), the gauge-invariant part of the exact TD PES $\varepsilon_{gi}(R,t)$ (blue solid), QSPESs $\varepsilon^{QS(1)}(R,t)$ (green solid) and $\varepsilon^{QS(2)}(R,t)$ (red solid), and the weighted average of the QSPESs $\varepsilon_{ave}^{QS}(R,t)$ (light blue solid) at indicated times. $|\chi_1^{QS}(R,t)|^2$ (green), $|\chi_2^{QS}(R,t)|^2$ (red) and $|\chi(R,t)|^2$ (orange) are also plotted.

This is plotted with light blue line in Fig. 3. Therefore the weighted-average of the QSPESs approximates the gauge-invariant part of exact TD PES $\varepsilon_{gi}(R,t)$, but not the full exact TD PES $\varepsilon(R,t)$. In fact, this is quite analogous to the previous results on the field-free passage through an avoided crossing^{52–54}: there, at the times considered, the density-weighted average collapsed to one BO surface or the other except in the intermediate (step) region, because the spatial separation of the parts of the density projected onto different BO surfaces meant that in the field-free analog to Eq. 30, the prefactors of each term was either one or zero. Here it is evident that the density does not spatially separate (Fig. 3), i.e. the projections on to the QSPESs overlap. One can make entirely analogous statements in both cases: the density-weighted average of the BOPES approximates the gauge-invariant part of exact TD PES $\varepsilon_{gi}(R,t)$ in the field-free case, and the density-weighted average of the QSPES approximates the gauge-invariant part of exact TD PES $\varepsilon_{gi}(R,t)$ in the presence of strong fields.

To confirm the relationship between $\varepsilon_{gi}(R,t)$ and $\varepsilon_{ave}^{QS}(R,t)$, we consider the expansion of the complete wavefunction with the two lowest quasi-static states (Eq. 10). Then the exact electronic

conditional wavefunction $\Phi_R(z, t)$ is expressed as:

$$\Phi_R(z, t) = \frac{\chi_1^{\text{QS}}(R, t)}{\chi(R, t)} \phi_R^{\text{QS}(1)}(z, t) + \frac{\chi_2^{\text{QS}}(R, t)}{\chi(R, t)} \phi_R^{\text{QS}(2)}(z, t). \quad (31)$$

Then we realize:

$$\begin{aligned} & \langle \Phi_R(z, t) | \hat{H}^{\text{BO}} + \hat{v}_{\text{laser}} | \Phi_R(z, t) \rangle_z \\ &= \frac{|\chi_1^{\text{QS}}(R, t)|^2}{|\chi(R, t)|^2} \varepsilon^{\text{QS}(1)} + \frac{|\chi_2^{\text{QS}}(R, t)|^2}{|\chi(R, t)|^2} \varepsilon^{\text{QS}(2)} \\ &= \varepsilon_{\text{ave}}^{\text{QS}}(R, t). \end{aligned} \quad (32)$$

Since $\varepsilon_{gi}(R, t) = \langle \Phi_R(z, t) | \hat{H}^{\text{BO}} + \hat{v}_{\text{laser}} | \Phi_R(z, t) \rangle_z + \frac{1}{2M} \langle \Phi_R(z, t) | (-i \frac{\partial}{\partial R} - A(R, t))^2 | \Phi_R(z, t) \rangle_z$, we can conclude

$$\varepsilon_{gi}(R, t) \approx \varepsilon_{\text{ave}}^{\text{QS}}(R, t), \quad (33)$$

because $O(M^{-1})$ term gives a much smaller contribution.

To reproduce the correct dynamics, however the effect of $\varepsilon_{gd}(R, t)$ is crucial to include, as in the field-free case studied before⁵⁴. In the gauge we have chosen $A(R, t) = 0$, but we note that if instead we choose the gauge where $\varepsilon_{gd}(R, t) = 0$ then the vector potential $A(R, t)$ will be non-zero, and will be responsible for the role of effectively reducing the oscillatory structure in the GI term.

In Fig. 4, we plot the gradient of the different potentials computed on the trajectory of mean nuclear distance $\langle R \rangle(t)$, as a more direct probe of the force on the nuclei. The black line, which is

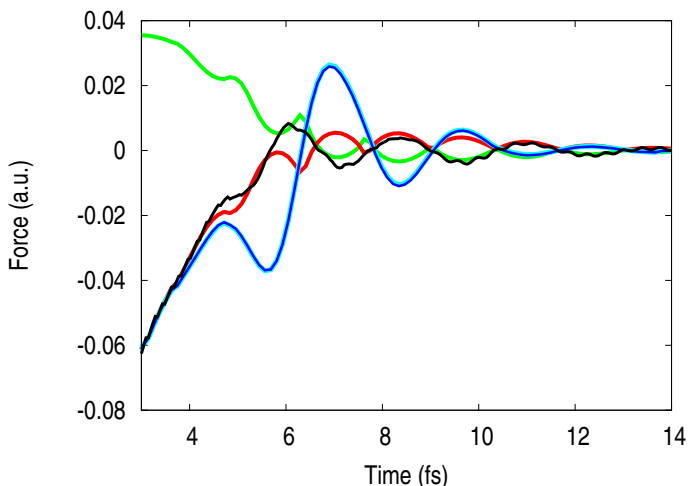


Fig. 4 Time evolution of the gradient of each TDPEs at position $\langle R(t) \rangle$. Green line: $\frac{\partial}{\partial R} \varepsilon^{\text{QS}(1)}(\langle R(t) \rangle)$; Red line: $\frac{\partial}{\partial R} \varepsilon^{\text{QS}(2)}(\langle R(t) \rangle)$; Blue line: $\frac{\partial}{\partial R} \varepsilon_{gi}(\langle R(t) \rangle)$; Light blue line: $\frac{\partial}{\partial R} \varepsilon_{\text{ave}}^{\text{QS}}(\langle R(t) \rangle)$; Black line: $\frac{\partial}{\partial R} \varepsilon(\langle R(t) \rangle)$.

the gradient of the exact TDPEs $\frac{\partial}{\partial R} \varepsilon(\langle R(t) \rangle)$, gives the exact force on the nuclei. First we immediately notice that the gradient of the weighted average of the two QSPES $\frac{\partial}{\partial R} \varepsilon_{\text{ave}}^{\text{QS}}(\langle R(t) \rangle)$ (light blue line) (equivalently, the GI component (blue line)) is completely different from the exact force. A semi-classical simulation on the weighted average of the two QSPES would not give the correct nuclear dynamics. We observe instead that, as the localization sets in, the exact force $\frac{\partial}{\partial R} \varepsilon(\langle R(t) \rangle)$ coincides with the gradient of

one or the other QSPES (red or green). This supports the idea of semiclassical surface-hopping between QSPES^{13,37,38} at least after the localization begins to set in (time ~ 6 fs): the exact force on the nuclei is given by the gradient of the exact TDPEs, and, when evaluated at the mean nuclear position, coincides with the force from one QSPES or the other, making transitions between them at their avoided crossings. This explains why the semiclassical simulations of Ref.¹³ had a reasonable agreement with the exact results. Furthermore the figure shows the important role of the gauge-dependent part $\varepsilon_{gd}(R, t)$; without this term, the force on the nuclei would be more oscillatory and quite different (blue line in the figure). We note that if instead we choose the gauge where $\varepsilon_{gd}(R, t) = 0$ then the vector potential $A(R, t)$ will be responsible for the role of effectively reducing the oscillatory structure in the GI term. As stated above, when we choose the gauge where $\varepsilon_{gd}(R, t) = 0$, then the vector potential $A(R, t)$ plays the role of it according to their relationship: $\tilde{A}(R, t) = \int_0^t dt' (-\partial_R \varepsilon_{gd}(R, t'))$ ⁵⁴.

3.3 Multiple trajectory Ehrenfest dynamics

Given that there are several avoided crossings during the localization dynamics, one might ask how well a mean-field surface to propagate the electrons would work. To this end, we run a multiple-trajectory Ehrenfest calculation*, and compare the electron and nuclear densities with the exact ones.

In the upper panel of Fig. 5, we plot the conditional electron density $|\Phi_R(z, t)|^2$ obtained from the exact calculation at indicated times. In the lower panel, we plot its squared expansion coefficients in the Born-Oppenheimer expansion $|C_g(R, t)|^2$ (green) and $|C_u(R, t)|^2$ (red) ($\Phi_R(z, t) = C_g(R, t)\Phi_R^g(z) + C_u(R, t)\Phi_R^u(z)$), along with the nuclear density (black). In Fig. 6, we plot the electron density $|\Phi(z, t|R_{cl}(t))|^2$ obtained from the 800-trajectory Ehrenfest dynamics calculation at the indicated times. The lower panel shows the squared expansion coefficients in the Born-Oppenheimer expansion $|C_g(R_{cl}(t))|^2$ (green) and $|C_u(R_{cl}(t))|^2$ (red) of the electronic wave function $\Phi(z, t|R_{cl}(t))$ obtained from multiple trajectory Ehrenfest dynamics calculation ($\Phi(z, t|R_{cl}(t)) = C_g(R_{cl}(t))\Phi_R^g(z) + C_u(R_{cl}(t))\Phi_R^u(z)$). We also show the nuclear densities reconstructed from the distribution of classical trajectories obtained from multiple trajectory Ehrenfest dynamics calculation (black circle line). Note that the 800 Ehrenfest trajectories cover the configuration space only partially. Hence, the reconstructed quantities equivalent to the fully quantum mechanical quantities can only be represented in a certain range in the configuration space that the trajectories cover at each instance of time. In Fig. 6, at $t = 4.8$ fs only $4.9\text{a.u.} < R < 6.6\text{a.u.}$ is covered while at $t = 12.0$ fs, the covered range is $7.5\text{a.u.} < R < 15\text{a.u.}$

* A set of 800 trajectories is propagated according to

$$\mu_n \frac{d}{dt} v_{cl}(t) = - \int dz \Phi(z, t|R_{cl}(t)) \left(\frac{d}{dR} \hat{H}_R^{\text{int}} \right) \Phi(z, t|R_{cl}(t)) \quad (34)$$

and

$$i \frac{\partial}{\partial t} \Phi(z, t|R_{cl}(t)) = \hat{H}_R^{\text{int}}(z, t) \Phi(z, t|R_{cl}(t)), \quad (35)$$

where the initial conditions are sampled from the phase-space distribution corresponding to $|\chi(R, t=0)\rangle^2$.

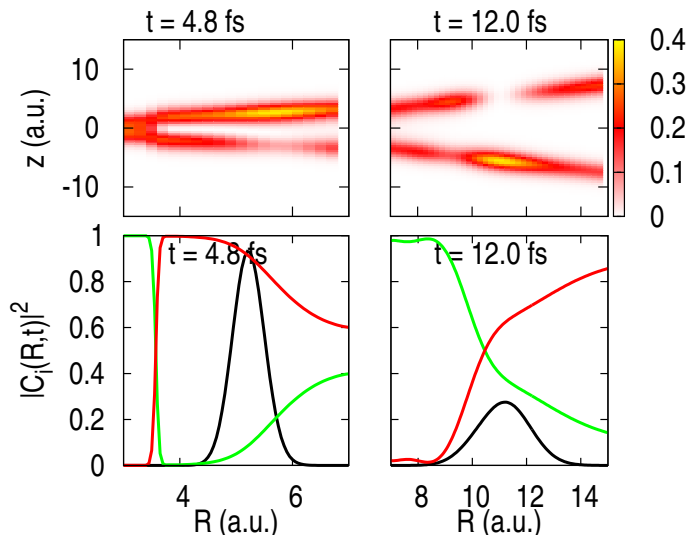


Fig. 5 Upper panel: Conditional electron density $|\Phi_R(z,t)|^2$ obtained from the exact calculation at the indicated times. Lower panel: Squared expansion coefficients of the Born-Oppenheimer expansion $|C_g(R,t)|^2$ (green) and $|C_u(R,t)|^2$ (red) of the exact conditional electronic wave function $\Phi_R(z,t)$ ($\Phi_R(z,t) = C_g(R,t)\Phi_R^g(z) + C_u(R,t)\Phi_R^u(z)$) at the indicated times. The exact nuclear density is also plotted (black).

Comparison of the top panels of Fig. 5 and Fig. 6 shows that the multiple-trajectory Ehrenfest dynamics captures the overall structure of the conditional electronic density, however the projections onto the BO states shown in the lower panels reveal there are substantial differences between them after several non-adiabatic transitions occur (at $t = 12.0$ fs). The difference is large especially for the regions where the nuclear density is small ($R < 10$ a.u. and $R > 12$ a.u.), but there are also noticeable differences where the nuclear density is peaked. For example, at $t = 12.0$ fs at $R \approx 11$ a.u., $|C_g(R_{cl}(t))|^2$ and $|C_u(R_{cl}(t))|^2$ shown in the lower panel of Fig. 6, are each close to 0.5, while the exact $|C_g(R,t)|^2$ and $|C_u(R,t)|^2$ shown in the lower panel of Fig. 5 are closer to 0.6 and 0.4, respectively. From the expressions of the BO g and u states in terms of the left and right basis (Sec. 2.1), we can see that the localization asymmetry predicted by Ehrenfest is close to 1:0 while the full quantum calculation predicts 0.8:0.2. Indeed this is verified by the calculation of the asymmetry of Ref.⁵⁶. Further, throughout the width of the nuclear wavepacket, the Ehrenfest projections remain close to 0.5, while the exact projections fall away. The differences in the conditional wavefunction and the BO projections are even greater where the nuclear density is small ($R = 7.5 \sim 10$ and $R = 12 \sim 15$).

In recent work, a new coupled-trajectory mixed quantum-classical approach based on the exactly factorized TDSE (Eqs (17) and (18)), has been presented⁶⁴, in which the equations take an Ehrenfest-like form but with important corrections that overcome limitations of Ehrenfest. In the field-free problem of non-adiabatic charge-transfer studied in that work^{52-54,64-67}, failure of multiple-trajectory Ehrenfest dynamics is expected given the fact that the nuclear density bifurcates spatially, and the corrections terms of Ref.⁶⁴ accurately captured the branching of the nuclear wavepacket as well as electronic decoherence. In the

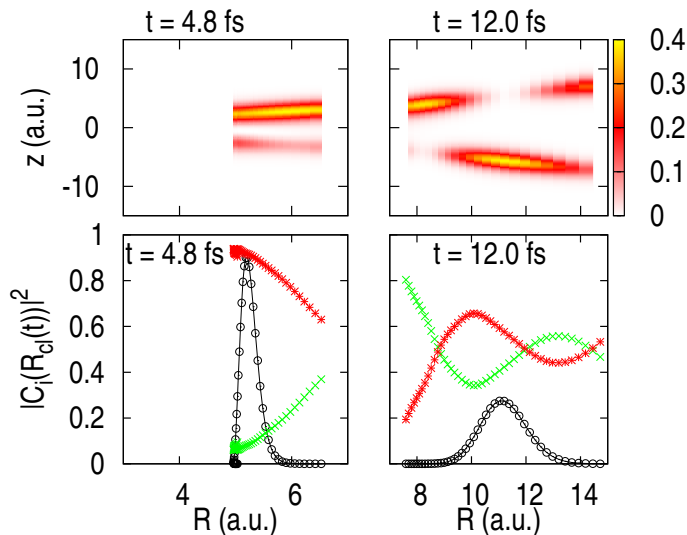


Fig. 6 Upper panel: Electron density $|\Phi(z,t|R_{cl}(t))|^2$ obtained from multiple trajectory Ehrenfest dynamics calculation at the indicated times (plotted for all trajectories $R_{cl}(t)$). Lower panel: Squared expansion coefficients of the Born-Oppenheimer expansion $|C_g(R_{cl}(t))|^2$ (green) and $|C_u(R_{cl}(t))|^2$ (red) of the electronic wave function $\Phi(z,t|R_{cl}(t))$ obtained from multiple trajectory Ehrenfest dynamics calculation ($\Phi(z,t|R_{cl}(t)) = C_g(R_{cl}(t))\Phi_R^g(z) + C_u(R_{cl}(t))\Phi_R^u(z)$) at the indicated times. Nuclear density reconstructed from the distribution of classical trajectories are also plotted (black circle line).

present case, however, the nuclear density does not split and is rather localized in space and the nuclear dynamics is overall well described by the Ehrenfest method. The nuclear density is very small where the difference in the conditional electron density is large ($R = 7.5 \sim 10$ and $R = 12 \sim 15$), thus, these differences do not affect the dynamics very much. But, still the errors in the electronic dynamics are noticeable, as discussed above in the BO projections and their implied localization asymmetry. This is consistent with the difference between the electronic potential in the Ehrenfest method and the exact potential (e -TD PES) acting on the electronic system, as defined within the inverse factorization^{56,68}.

4 Conclusions and Outlook

The TD PES and vector potential arising from the exact factorization of the molecular wavefunction exactly account for the coupling to the electronic subsystem as well as coupling to external fields and so it is important to understand their structure, and to relate this to the QSPES which is traditionally used, in order to be able to develop accurate practical mixed quantum-classical methods for strong-field dynamics. In this paper, we have studied the topical phenomenon of laser-induced electron localization in the dissociation of H_2^+ , choosing a gauge where the TD PES is only potential acting on the nuclear system. We found that the gauge-independent component of the TD PES has a mean-field-like character very close to the density-weighted average of the QSPESs and yields an oscillatory force on the nuclei. The gauge-dependent component of the TD PES smoothens the oscillations of the gauge-independent component and together they lead to the correct force.

We demonstrated that running an ensemble of classical nuclear

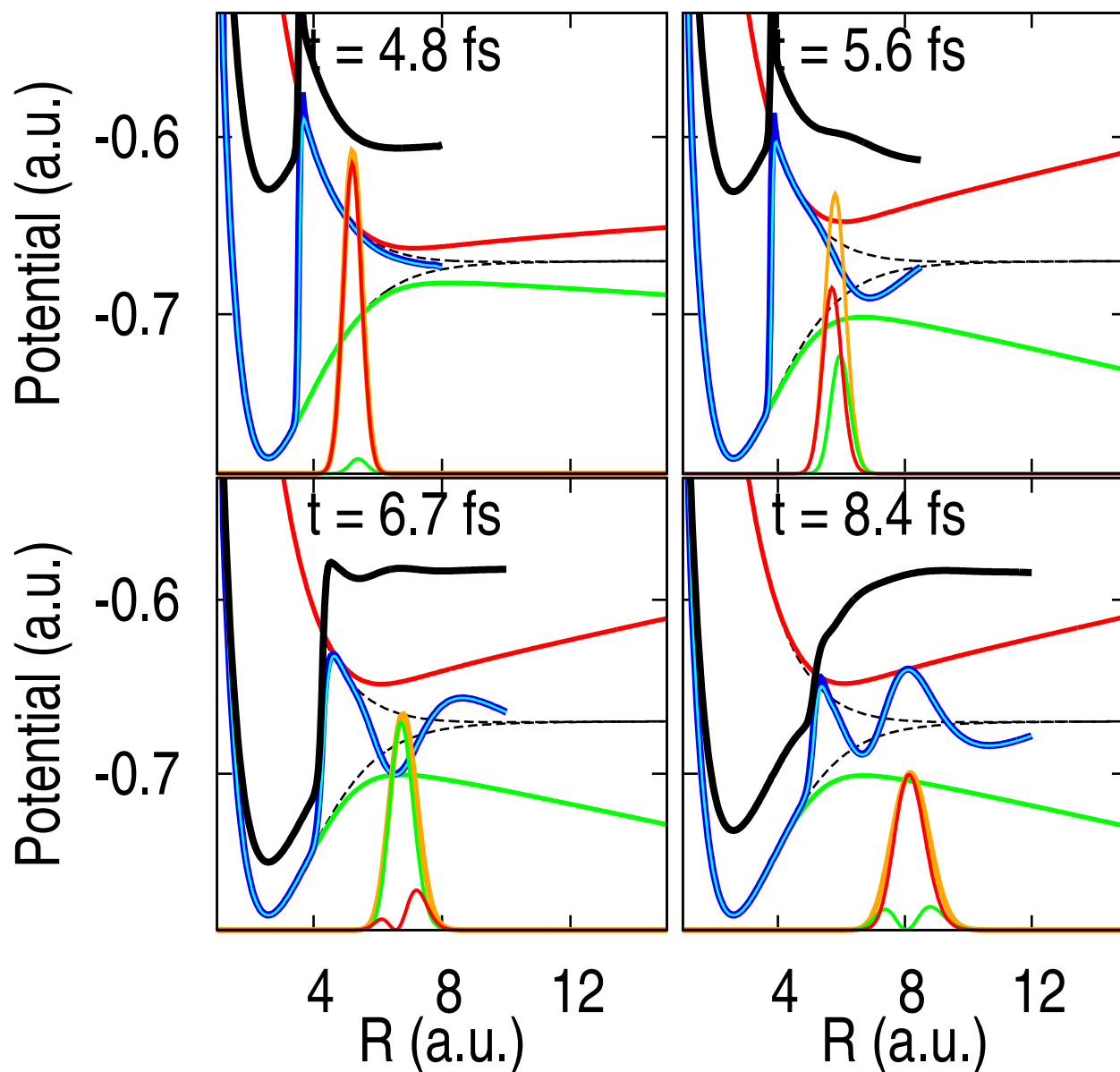
trajectories on this exact TDPEs accurately reproduces the exact nuclear dynamics. We found that the force obtained by considering surface-hopping transitions between QSPESs at the laser-induced avoided crossing approximates this exact force, after the localization begins to set in. We showed that errors in multiple-trajectory Ehrenfest dynamics are less significant for the nuclear dynamics than for the electronic dynamics explored in Ref.⁵⁶, where it was shown that Ehrenfest yields an incorrect electron localization asymmetry. It is worth noting that the potential acting on the electrons in Ehrenfest dynamics and in surface-hopping schemes lack important step and peak features that the exact potential acting on the electronic system (the *e*-TDPEs) has. Therefore the results of this study show that to reproduce the laser-induced electron localization dynamics accurately by means of a mixed quantum-classical dynamics scheme, we have to go beyond the traditional methods such as surface-hopping or Ehrenfest methods. Our results here encourage the development of mixed quantum-classical schemes based on Eqs (17) and (18)⁶⁴ to simulate strong-field processes.

Acknowledgments: Partial support from the Deutsche Forschungsgemeinschaft (SFB 762), the European Commission (FP7-NMP-CRONOS), and the U.S. Department of Energy, Office of Basic Energy Sciences, Division of Chemical Sciences, Geosciences and Biosciences under award DE-SC0008623 (NTM), is gratefully acknowledged.

References

- 1 F. Krausz and M. Ivanov, *Rev. Mod. Phys.*, 2009, **81**, 163.
- 2 M. J. J. Vrakking, *Phys. Chem. Chem. Phys.*, 2014, **16**, 2775.
- 3 F. Lépine, M. Y. Ivanov and M. J. J. Vrakking, *Nature Photon.*, 2014, **8**, 195.
- 4 S. Haessler *et al.*, *Nature Phys.*, 2010, **6**, 200.
- 5 P. B. Corkum and F. Krausz, *Nature Phys.*, 2007, **3**, 381.
- 6 F. Calegari *et al.*, *Science*, 2014, **346**, 336.
- 7 G. Sansone *et al.*, *Nature*, 2010, **465**, 763.
- 8 F. He, C. Ruiz and A. Becker, *Phys. Rev. Lett.*, 2007, **99**, 083002.
- 9 D. Ray *et al.*, *Phys. Rev. Lett.*, 2009, **103**, 223201.
- 10 K. P. Singh *et al.*, *Phys. Rev. Lett.*, 2010, **104**, 023001.
- 11 B. Fischer *et al.*, *Phys. Rev. Lett.*, 2010, **105**, 223001.
- 12 C. R. Calvert *et al.*, *J. Phys. B: At. Mol. Opt. Phys.*, 2010, **43**, 011001.
- 13 F. Kelkensberg, G. Sansone, M. Y. Ivanov and M. Vrakking, *Phys. Chem. Chem. Phys.*, 2011, **13**, 8647.
- 14 F. He, *Phys. Rev. A*, 2012, **86**, 063415.
- 15 K. Liu, Q. Zhang and P. Lu, *Phys. Rev. A*, 2012, **86**, 033410.
- 16 Z. Jia, Z. Zeng, R. Li, Z. Xu and Y. Deng, *Phys. Rev. A*, 2014, **89**, 023419.
- 17 Z. Wang, K. Liu, P. Lan and P. Lu, *Phys. Rev. A*, 2015, **91**, 043419.
- 18 M. F. Kling *et al.*, *Science*, 2006, **312**, 246.
- 19 M. Kremer *et al.*, *Phys. Rev. Lett.*, 2009, **103**, 213003.
- 20 V. Roudnev, B. D. Esry and I. Ben-Itzhak, *Phys. Rev. Lett.*, 2004, **93**, 163601.
- 21 X. M. Tong and C. D. Lin, *Phys. Rev. Lett.*, 2007, **98**, 123002.
- 22 S. Graefe and M. Y. Ivanov, *Phys. Rev. Lett.*, 2007, **99**, 163603.
- 23 T. Rathje *et al.*, *Phys. Rev. Lett.*, 2013, **111**, 093002.
- 24 N. G. Kling *et al.*, *Phys. Rev. Lett.*, 2013, **111**, 163004.
- 25 H. Li *et al.*, *J. Phys. B: At. Mol. Opt. Phys.*, 2014, **47**, 124020.
- 26 P. Lan, E. J. Takahashi and K. Midorikawa, *Phys. Rev. A*, 2012, **86**, 013418.
- 27 M. Kübel *et al.*, *New J. Phys.*, 2014, **16**, 065017.
- 28 H. Li *et al.*, *Phys. Rev. Lett.*, 2015, **114**, 123004.
- 29 R. Mitrić, J. Peterson and V. Bonačić-Koutecký, *Phys. Rev. A*, 2009, **79**, 053416.
- 30 I. Tavernelli, B. F. E. Curchod and U. Rothlisberger, *Phys. Rev. A*, 2010, **81**, 052508.
- 31 M. Richer, P. Marquetand, J. González-Vázquez, I. Sola and L. González, *J. Chem. Theory Comput.*, 2011, **7**, 1253.
- 32 J. J. Bajo, J. González-Vázquez, I. Sola, J. Santamaria, M. Richer, P. Marquetand, and L. González, *J. Phys. Chem. A*, 2012, **116**, 2800.
- 33 J. C. Tully, *J. Chem. Phys.*, 1990, **93**, 1061.
- 34 S. Hammes-Schiffer and J. C. Tully, *J. Chem. Phys.*, 1994, **101**, 4657.
- 35 J. C. Tully, *Faraday Discuss.*, 1998, **110**, 407.
- 36 P. Dietrich, M. Y. Ivanov, F. A. Ilkov and P. B. Corkum, *Phys. Rev. Lett.*, 1996, **77**, 4150.
- 37 M. Thachuk, M. Y. Ivanov and D. M. Wardlaw, *J. Chem. Phys.*, 1996, **109**, 4094.
- 38 M. Thachuk, M. Y. Ivanov and D. M. Wardlaw, *J. Chem. Phys.*, 1998, **109**, 5747.
- 39 N. Shenvi, J. E. Subotnik and W. Yang, *J. Chem. Phys.*, 2011, **134**, 144102.
- 40 A. W. Jasper, S. Nangia, C. Zhu and D. G. Truhlar, *Acc. Chem. Res.*, 2006, **39**, 101.
- 41 E. R. Bittner and P. J. Rossky, *J. Chem. Phys.*, 1995, **103**, 8130.
- 42 A. V. Akimov, R. Long and O. V. Prezhdo, *J. Chem. Phys.*, 2014, **140**, 194107.
- 43 B. F. E. Curchod and I. Tavernelli, *J. Chem. Phys.*, 2013, **138**, 184112.
- 44 N. Makri, *Chem. Phys. Lett.*, 2014, **593**, 93.
- 45 R. Grunwald, H. Kim and R. Kapral, *J. Chem. Phys.*, 2008, **128**, 164110.
- 46 G. Granucci and M. Persico, *J. Chem. Phys.*, 2007, **126**, 134114.
- 47 A. Abedi, N. T. Maitra and E. K. U. Gross, *Phys. Rev. Lett.*, 2010, **105**, 123002.
- 48 A. Abedi, N. T. Maitra and E. K. U. Gross, *J. Chem. Phys.*, 2012, **137**, 22A530.
- 49 A. Scherrer, F. Agostini, D. Sebastiani, E. K. U. Gross and R. Vuilleumier, *J. Chem. Phys.*, 2015, **143**, 074106.
- 50 S. K. Min, A. Abedi, K. S. Kim and E. K. U. Gross, *Phys. Rev. Lett.*, 2014, **113**, 263004.
- 51 R. Requist and E. K. U. Gross, *arXiv:1506.09193*, 2015.
- 52 A. Abedi, F. Agostini, Y. Suzuki and E. K. U. Gross, *Phys. Rev. Lett.*, 2013, **110**, 263001.

- 53 F. Agostini, A. Abedi, Y. Suzuki and E. K. U. Gross, *Mol. Phys.*, 2013, **111**, 3625.
- 54 F. Agostini, A. Abedi, Y. Suzuki, S. K. Min, N. T. Maitra and E. K. U. Gross, *J. Chem. Phys.*, 2015, **142**, 084303.
- 55 S. Shin and H. Metiu, *J. Chem. Phys.*, 1995, **102**, 23.
- 56 Y. Suzuki, A. Abedi, N. T. Maitra, K. Yamashita and E. K. U. Gross, *Phys. Rev. A*, 2014, **89**, 040501(R).
- 57 P. Dietrich and P. B. Corkum, *J. Chem. Phys.*, 1992, **97**, 3187.
- 58 T. Zuo and A. Bandrauk, *Phys. Rev. A*, 1995, **52**, R2511.
- 59 T. Seideman, M. Y. Ivanov and P. B. Corkum, *Phys. Rev. Lett.*, 1995, **75**, 2819.
- 60 I. Kawata, H. Kono and Y. Fujimura, *Chem. Phys. Lett.*, 1998, **289**, 546.
- 61 I. Kawata, H. Kono and Y. Fujimura, *J. Chem. Phys.*, 1999, **110**, 11152.
- 62 H. Kono *et al.*, *Chem. Phys.*, 2004, **304**, 203.
- 63 T. Kato, H. Kono, M. Kanno, Y. Fujimura and K. Yamanouchi, *Laser Phys.*, 2009, **19**, 1712.
- 64 S. K. Min, F. Agostini and E. K. U. Gross, *Phys. Rev. Lett.*, 2015, **115**, 073001.
- 65 A. Abedi, F. Agostini and E. K. U. Gross, *Euro. Phys. Lett.*, 2014, **106**, 33001.
- 66 F. Agostini, A. Abedi and E. K. U. Gross, *J. Chem. Phys.*, 2014, **141**, 214101.
- 67 F. Agostini, S. K. Min and E. K. U. Gross, *Ann. Phys.*, 2015, published online.
- 68 E. Khosravi, A. Abedi and N. T. Maitra, *arXiv:1508.01414*, 2015.



The exact nuclear time-dependent potential energy surface for laser-induced electron localization is studied with a view to developing a mixed quantum-classical dynamics method for strong-field processes.